

# Reflection tomography of time-lapse GPR data for studying dynamic unsaturated flow phenomena

Adam R. Mangel<sup>1,2</sup>, Stephen M.J. Moysey<sup>2</sup>, John Bradford<sup>1</sup>

<sup>1</sup> Department of Geophysics, Colorado School of Mines, Golden, Colorado, 80401, USA

<sup>2</sup> Department of Environmental Engineering and Earth Science, Clemson University, Clemson, South Carolina, 29634, USA

Corresponding to: Adam R. Mangel (amangel@mines.edu)

## Abstract

Ground-penetrating radar (GPR) reflection tomography algorithms allow non-invasive monitoring of water content changes resulting from flow in the vadose zone. The approach requires multi-offset GPR data that is traditionally slow to collect. We automate GPR data collection to reduce the survey time significantly, thereby making this approach to hydrologic monitoring feasible. The method was evaluated using numerical simulations and laboratory experiments that suggest reflection tomography can provide water content estimates to within 5-10% vol./vol. for the synthetic studies, whereas the empirical estimates were typically within 5-15% of measurements from in-situ probes. Both studies show larger observed errors in water content near the periphery of the wetting front, beyond which additional reflectors were not present to provide data coverage. Overall, coupling automated GPR data collection with reflection tomography provides a new method for informing models of subsurface hydrologic processes and a new method for determining transient 2D soil moisture distributions.

## 1. Introduction

Preferential flow is ubiquitous in the vadose zone, occurring under a wide variety of conditions and over a broad range of scales (Nimmo, 2012). Reviews such as those by Hendrickx and Flury (2001) and Jarvis (2007) illustrate that a basic mechanistic understanding of preferential flow exists. Jarvis et al. (2016) point out, however, that we still lack models capable of reproducing empirical observations in the field and highlight the importance of non-invasive imaging techniques for improving this understanding. We suggest that ground-penetrating radar (GPR) reflection tomography could fill this need by quantitatively mapping changes in water content through space and time at the sub-meter scale.

Reflection GPR is commonly used to image subsurface structures, but is also well suited to understanding hydrologic variability due to the strong dependence of EM wave velocities on soil volumetric water content (Topp et al., 1980). As a result, GPR has been adapted to monitor variability in hydrologic processes at multiple scales through time and space in a variety of contexts (Buchner et al., 2011; Busch et al., 2013; Guo et al., 2014; Haarder et al., 2011; Lunt et al., 2005; Mangel et al., 2012, 2015b, 2017; Moysey, 2010; Sautenoy et al., 2007; Steelman and Endres, 2010; Vellidis et al., 1990). Note that GPR methods are not applicable in media with relatively high electrical conductivity.

While these studies have illustrated a variety of techniques for monitoring changes in water content within the subsurface, they have generally required assumptions to constrain the interpretation, such as the use of *a priori* information regarding subsurface structure (e.g., Lunt et al., 2005) or the GPR wave velocity (Haarder et al., 2011).

37 These limitations arise from the fact that GPR data are recorded as energy arriving at the receiver antenna as a function  
38 of time. Inherent assumptions therefore exist in analyzing traveltime data collected with antennas separated by a fixed  
39 offset because both the distance travelled by the GPR wave to a reflector and the velocity of the GPR wave are  
40 unknown. It has been demonstrated that GPR data collected via a multi-offset survey can constrain both the depth to  
41 a moving wetting front and the water content behind the front over the course of an infiltration event (Gerhards et al.,  
42 2008; Mangel et al., 2012). The limitation of these studies, however, was that the authors assumed a 1D flow system  
43 and that GPR data lacked information regarding lateral variability in soil moisture.

44 Extending multi-offset techniques (Forte and Pipan, 2017; Jaumann and Roth, 2017; Klenk et al., 2015;  
45 Lambot et al., 2004, 2009) to image flow in the vadose zone requires an increase in the speed at which these data can  
46 be collected and advanced processing methods that can combine thousands of measurements into spatially and  
47 temporally variable water content estimates. We have recently overcome the data collection problem by automating  
48 GPR data collection using a computer controlled gantry, thereby reducing the data collection time for large multi-  
49 offset surveys from hours to minutes (Mangel et al., 2015a). Tomography and wave migration algorithms from  
50 seismic literature have been available for decades (Baysal et al., 1983; Lafond and Levander, 1993; Sava and Biondi,  
51 2004a, 2004b; Stork, 1992; Yilmaz and Chambers, 1984) and are being continually adapted to GPR applications. For  
52 example, this work is made possible due to adaptation of the pre-stack migration algorithm (Leparoux et al., 2001)  
53 and adaptation of the reflection tomography algorithm (Bradford, 2006) to multi-offset GPR data. Subsequent studies  
54 have demonstrated the use of GPR reflection tomography for imaging static distributions of subsurface water content  
55 with great detail (Bradford, 2008; Bradford et al., 2009; Brosten et al., 2009). The combination of automated GPR  
56 data collection and reflection tomography makes time-lapse imaging of water content during infiltration a feasible  
57 means to study flow in the vadose zone.

58 The objective of this study is to evaluate reflection tomography of high-resolution GPR data as a tool for  
59 observing and characterizing unsaturated flow patterns during infiltration into a homogeneous soil. To evaluate the  
60 efficacy of the algorithm for resolving dynamic soil water content in 2D, we first test the algorithm using numerical  
61 simulations and compare the results to true water content distributions. We then apply the algorithm to time-lapse  
62 GPR data collected during an infiltration and recovery event in a homogeneous soil and compare results to  
63 measurements from in-situ soil moisture probes.

## 64 **2. Methods**

### 65 **2.1. The Reflection Tomography Algorithm**

66 The goal of reflection tomography is to determine a velocity model that best aligns migrated reflection  
67 arrivals for a common reflection point across a set of source-receiver offsets. For brevity, we will limit our discussion  
68 here to the key ideas and methods of the tomography algorithm; we refer the reader to Stork (1992) for the original  
69 tomography algorithm and to Bradford (2006) for the application to GPR data.

70 The data required for this algorithm are an ensemble of common-midpoint (CMP) gathers collected along a  
71 path. Given that GPR data is a time-series record of electromagnetic energy arriving at a point in space, we must  
72 know the proper velocity structure to migrate the data and produce a depth registered image of the GPR energy.  
73 Migration attempts to remove the hyperbolic trend of reflections with respect to antenna offset (Figure 1a) by using

74 the wave velocity to reposition reflections to the proper depth at which they occur. If CMP data are migrated with the  
75 correct velocity, reflections from layers in the subsurface are flattened as a function of offset (Fig. 1c). If the velocity  
76 estimate is incorrect, e.g. 10% too slow (Fig. 1b) or 10% too fast (Fig. 1d), the arrival is not flat and exhibits residual  
77 moveout (RMO). To solve for the velocity structure and properly migrate the data, the reflection tomography  
78 algorithm proceeds as follows (Bradford, 2006; Stork, 1992):

- 79 1. Generate a starting depth vs. velocity model.
- 80 2. Migrate the data with the starting velocity model and stack the data.
- 81 3. Pick horizons on the stacked image.
- 82 4. Perform ray-tracing to the picked horizons with the velocity model.
- 83 5. Evaluate horizons for residual moveout.
- 84 6. Adjust velocity model using reflection tomography.
- 85 7. Apply revised velocity model using migration and quality check RMO.
- 86 8. Iterate at step three if necessary.

87 For this work, starting velocity models for the tomography algorithm are determined by smoothing results  
88 from 1D velocity analysis of individual CMPs (Neidell and Taner, 1971). The reflection tomography algorithm then  
89 adjusts the velocity distribution until reflections in the depth corrected (i.e., migrated) data line up to produce a  
90 reflection at a consistent depth across all traces in a CMP. Through sequential iterations of the tomographic inversion,  
91 the RMO metric is reduced on a global scale. For this work, the reflection tomography was performed using the  
92 SeisWorks software suite and Kirchhoff pre-stack depth migration (Yilmaz and Doherty, 2001).

## 93 **2.2. Experimental Setup and Procedure**

94 We used a 4 m x 4 m x 2 m tank for the controlled study of unsaturated flow phenomenon with GPR (Fig.  
95 1e, f). We filled the tank with a medium-grained sand to a depth of 0.60 m. Below the sand was a 0.30 m layer of  
96 gravel that acts as backfill for 16 individual drain cells that are pitched slightly toward central drains that route water  
97 to outlets on the outside of the tank. We constructed an automated data collection system to allow for the high-speed  
98 high-resolution collection of GPR data (Mangel et al., 2015a); the GPR gantry fits inside of the tank so the antennas  
99 are in contact with the sand surface. All GPR data described here were collected along the y-axis of the tank at a fixed  
100 position of  $x = 2.0$  m, where the bottom of the tank is flat (Fig. 1e, f).

101 The automated system, which utilizes a 1000 MHz Sensors and Software bistatic radar (Sensors and  
102 Software, Inc.), was operated to obtain 101 CMPs spaced at 0.02 m intervals between  $y = 1.0 - 3.0$  m. Each CMP  
103 consisted of 84 traces with offsets between 0.16-1.0 m at 0.01 m step size. Thus, a complete CMP data set for one  
104 observation time consists of almost 8,500 individual GPR traces. With this configuration using the automated system,  
105 a CMP at a single location could be collected in 1.8 seconds with a total cycle of CMP data locations collected every  
106 3.9 minutes.

107 GPR data collection occurred prior to irrigation to evaluate background conditions. Data collection continued  
108 during irrigation, which was applied at a flux of 0.125 cm/min for a duration of 2.13 hrs. Spatial heterogeneity in the  
109 applied flux has been observed in laboratory testing of the irrigation equipment. Fifteen EC-5 soil moisture probes  
110 (METER, Inc.) logged volumetric water content at 10 second intervals during the experiment (Fig. 1e, f). Note that

111 the soil moisture probes are located out of the plane of the GPR line by 0.5 m (Figure 1f). GPR data collection  
112 continued for 40 min. after the irrigation was terminated. In total, 45 complete sets of data were collected over the  
113 course of the 3-hour experiment, yielding more than 500,000 GPR traces in the experimental data set.

### 114 **2.3. Execution of the Numerical Simulations**

115 We employed HYDRUS-2D (Simunek and van Genuchten, 2005) to simulate a theoretical and realistic  
116 hydrologic response to an infiltration event using two different initial conditions: i) hydrostatic equilibrium leading to  
117 a water content distribution controlled by the soil water retention curve, and ii) a uniform soil with a water content of  
118 0.07. We selected the Mualem-van Genuchten soil model (Mualem, 1976) and parameterized the model as follows  
119 based on hydraulic testing of the sand: residual water content ( $\theta_r$ ) = 0.06, saturated water content ( $\theta_s$ ) = 0.38, air-entry  
120 pressure ( $\alpha$ ) = 0.058 cm<sup>-1</sup>, shape parameter ( $n$ ) = 4.09, and saturated hydraulic conductivity ( $K_s$ ) = 4.6 cm min<sup>-1</sup>. The  
121 hydraulic conductivity for the homogeneous model was reduced to 1 cm min<sup>-1</sup> to build a larger contrast of water  
122 content across the wetting front. For all HYDRUS simulations, we used a constant flux boundary condition of 0.125  
123 cm/min from  $y = 1.6 - 2.4$  m along the ground surface, set the model domain depth to 0.6 m, length to 4.0 m, and  
124 nominal cell size to 0.04 m. Remaining nodes at the surface were set to no flow boundaries and lower boundary nodes  
125 were set to a seepage face with the pressure head equal to zero.

126 We calculated relative dielectric permittivity values for the GPR simulations by transforming water content values  
127 from HYDRUS-2D using the Topp equation (Topp et al., 1980). We used the magnetic permeability of free space for  
128 the entire model domain and set electrical conductivity of the soil to 1 mS/m. Although electrical conductivity changes  
129 as a function of the water content, these changes primarily influence wave attenuation, which is not significant or  
130 accounted for in the processing performed with the SeisWorks software.

131 We performed GPR simulations in MATLAB using a 2D finite-difference time-domain code (Irving and  
132 Knight, 2006). The GPR model domain was set to 4.0 m long and 1.1 m high with a cell size of 0.002 m. The lower  
133 0.3 m of the domain was set to a relative dielectric permittivity of 2.25 to represent the lower gravel layer and the  
134 upper 0.2 m was modeled as air to simulate the air-soil interface. Simulated data were collected as described in the  
135 section detailing the tank experiment. For quick computation, simulations were deployed on the Palmetto  
136 supercomputer cluster at Clemson University, where single source simulations ran in 20 minutes using nodes with 8  
137 CPUs and 32 GB of RAM.

### 138 **3. Reflection Tomography of Simulations**

139 The HYDRUS-2D output shows the development of an infiltrating wetting front for the two scenarios with  
140 differing initial conditions (Figs. 2a, f, k). For conditions prior to irrigation, the bottom of sand reflection (B) is  
141 horizontal on the common-offset profile (COP) data indicating a constant velocity across the model domain (Fig. 2b).  
142 Additionally, the CMPs show identical hyperbolic moveout, i.e., the offset vs. travelttime relationship, indicating a  
143 homogeneous velocity across the model domain (Fig. 2c-e). The airwave and groundwave are also visible in the data,  
144 but are not analyzed, or further discussed.

145 During infiltration, (B) is distorted at the center of the COP due to the decreased velocity caused by the  
146 infiltrating water (Figs. 2g, l). A reflection from the infiltrating wetting front (W) is faintly visible for the model with  
147 variable initial water contents (Fig. 2g) and comparatively strong for simulations with a dry background (Fig. 2l) due

148 to different levels of dielectric contrast across the wetting front in each case. CMPs also indicate perturbations in the  
149 velocity field as the moveout changes dramatically when the wetted zone is encountered (Figs. 2h-j, m-o). A refraction  
150 is also observed on the CMPs, which is a rare occurrence considering that GPR wave velocity typically decreases with  
151 depth.

152 Prior to the onset of flow, the reflection tomography algorithm produces a uniform water content distribution  
153 that agrees with the arithmetic average of the true water content but does not capture the vertical gradation observed  
154 in Figure 3a. This is because information regarding vertical velocity variations is absent, i.e., more reflectors at  
155 different depths are required to capture this variability. As a result, errors in the water content estimation exceed 10%  
156 vol./vol (Fig. 3d).

157 During infiltration the wetting front is imaged relatively well for the case where the soil was initially dry  
158 (Figs. 3i-l), particularly as the plume advances deeper into the subsurface (Figs. 3m-p) where there is improved data  
159 coverage. The tomography algorithm overestimates the depth of the wetting front by roughly 0.10 m for the case  
160 presented in Figure 3i-l, which is likely due to smoothing effects required to regularize the inversion or an error in the  
161 picking of the wetting front horizon. Considerable errors in the tomography results persist, however, with the results  
162 degrading further for the scenario with variable initial water content (Figs. 3e-h) given that reflection contrasts with  
163 the wetting front are weaker. The presence of an additional reflector, however, increases the ability of the tomography  
164 to resolve vertical variability, e.g. Figure 2g vs. Figure 2b. Overall, errors are reduced near reflectors to about 5%  
165 vol./vol. These results suggest that water content changes resulting from unsaturated flow can be imaged and that as  
166 more information becomes available in the form of additional reflections, the tomography results improve.

#### 167 **4. Reflection Tomography of Experimental Data**

168 At initial conditions, the sand layer reflection (B) is visible at 10 ns traveltimes in the COP collected over the  
169 imaging area (Fig. 4a). Normal hyperbolic moveout of (B) is observed on the CMPs (Fig.4b, c, d). These results are  
170 qualitatively identical to observations from numerical simulations (Figs. 2b-e).

171 During infiltration, the water content of the sand layer increases substantially (Fig. 5) and longer traveltimes  
172 of the arrivals on the COP data are observed near the center of the tank (Figs. 4f, i). Rather than a coherent reflection  
173 for the wetting front (W) (Fig. 2l), multiple discrete reflections are present in the COP data (Fig. 4e, i, m) indicating  
174 a heterogeneous wetting of the soil. These reflections are difficult to identify on the CMPs given the complex moveout  
175 pattern (Fig. 4i) but are more easily identified in animations of COP projections of the data (included as a  
176 supplementary file). Analysis of the data was greatly aided by the animation of the data and the pre-stack migration  
177 algorithm, which stacks the data over all offsets to produce a coherent image of reflectors with an increased signal to  
178 noise ratio. Heterogeneous wetting of the soil is also very pronounced in the soil-moisture probe data with many of  
179 the probes responding out of sequence with depth (Fig 5). After irrigation, the soil moisture probes show a decrease  
180 in the soil water content (Fig. 5) apart from one probe (Fig. 5c) and the GPR data show a slight decrease in the  
181 traveltimes of the bottom of sand reflection (Figs. 4k-n).

182 The tomographic imaging results from the initial GPR data set collected prior to irrigation agree with data  
183 from soil moisture probes which indicates an average soil moisture of roughly 5% during this time (Figs. 4e, 5).  
184 During infiltration and recovery, tomographic images of the tank show a wet zone at the center and relatively dry

185 edges outside the irrigated area (Figs. 4j, o). Overall, the tomography results near the center of the tank are within  
186 10% vol./vol. of the soil moisture data and show a non-uniform wetting of the soil during infiltration that was not  
187 observed in the numerical study, suggesting the occurrence of preferential flow. Errors in the estimates of water  
188 content near the edges of the advancing plume exceed 15% vol./vol. (Fig. 4b, c), though the general patterns in wetting  
189 are consistent. After irrigation, the tomography results on the edges of the wetted zone are in better agreement with  
190 the soil moisture probe data, but less spatial information is available given the lack of a wetting front reflection (Fig.  
191 4o).

## 192 **5. Conclusions**

193 Reflection tomography in the post-migrated domain is a viable method for resolving transient soil moisture  
194 content in 2D associated with an infiltration and recovery event in a homogeneous soil. Reflection tomography of  
195 numerical data produced water content distributions that were in good agreement with true water content values from  
196 the simulations. The tomography was generally able to match the true water content values to within 5-10% vol./vol.  
197 However, distinct migration artifacts were produced around the edges of the wetting front, especially for cases where  
198 the initial water content was non-uniform, obscuring details about the shape of the wetted region. Analysis of data  
199 collected in a sand tank proved to be more difficult, however, the tomography was able to produce hydrologically  
200 realistic distributions of water content in space and time that were generally within 5-15% vol./vol. of measurements  
201 from in-situ soil moisture probes. This may have to do with the complex distribution of the wetted soil as a result of  
202 heterogenous distribution of water at the surface, texture variability in the soil, or other preferential flow mechanisms  
203 (Jarvis et al., 2016). Regardless, the fact that the GPR data were able to capture this heterogeneity is an impressive  
204 feat given that tomographic imaging operated independently of any hydrologic information and provided evidence  
205 that our conceptual model was not representative of the physical system.

206 Regardless of discrepancies observed between the GPR and probe water content values, it is evident that  
207 automated high-speed GPR data acquisition coupled with reflection tomography algorithms can provide a new  
208 approach to hydrologic monitoring. Testing and revision of conceptual hydrologic models regarding non-uniform  
209 flow in the vadose zone demands such non-invasive time-lapse imaging data. Artifacts observed in the numerical  
210 simulation results, however, suggest that improvements in this methodology could be achieved. While there are likely  
211 fundamental limitations to the information content of the data, the Kirchhoff pre-stack depth migration algorithm used  
212 in this study could be replaced by more sophisticated algorithms like reverse-time migration (Baysal et al., 1983)  
213 which may reduce the observed imaging artifacts. Additionally, results from the tomography algorithm may prove to  
214 be beneficial as a precursor to higher-order inversion techniques, like full-waveform inversion, which requires detailed  
215 starting models of velocity for convergence. Overall, coupling automated GPR data collection with reflection  
216 tomography provides a new method for informing models of subsurface hydrologic processes and a new method for  
217 determining transient 2D soil moisture distributions.

## 218 **6. Acknowledgements**

219 This material is based upon work supported by, or in part by, the National Science Foundation under grant  
220 number EAR-1151294. We also acknowledge Clemson University for generous allotment of compute time on

221 Palmetto cluster. Data used in this publication and a supplementary movie of the data are available through the  
222 Colorado School of Mines at the following URL: <https://hdl.handle.net/11124/172053>.

## 223 7. References

224 Baysal, E., Kosloff, D. and Sherwood, J.: Reverse Time Migration, *Geophysics*, 48(11), 1514–1524,  
225 doi:10.1190/1.1441434, 1983.

226 Bradford, J. H.: Applying reflection tomography in the postmigrated domain to multifold ground-penetrating radar  
227 data, *Geophysics*, 71(1), K1–K8, doi:10.1190/1.2159051, 2006.

228 Bradford, J. H.: Measuring Water Content Heterogeneity Using Multifold GPR with Reflection Tomography, *Vadose*  
229 *Zo. J.*, 7(1), 184, doi:10.2136/vzj2006.0160, 2008.

230 Bradford, J. H., Clement, W. P. and Barrash, W.: Estimating porosity with ground-penetrating radar reflection  
231 tomography: A controlled 3-D experiment at the Boise Hydrogeophysical Research Site, *Water Resour. Res.*, 45(4),  
232 n/a-n/a, doi:10.1029/2008WR006960, 2009.

233 Brosten, T. R., Bradford, J. H., McNamara, J. P., Gooseff, M. N., Zarnetske, J. P., Bowden, W. B. and Johnston, M.  
234 E.: Multi-offset GPR methods for hyporheic zone investigations, *Near Surf. Geophys.*, 7, 244–257, 2009.

235 Buchner, J. S., Kuhne, A., Antz, B., Roth, K. and Wollschlager, U.: Observation of volumetric water content and  
236 reflector depth with multichannel ground-penetrating radar in an artificial sand volume, 2011 6th Int. Work. Adv. Gr.  
237 Penetrating Radar, 1–5, doi:10.1109/IWAGPR.2011.5963910, 2011.

238 Busch, S., Weihermüller, L., Huisman, J. A., Steelman, C. M., Endres, A. L., Vereecken, H. and van der Kruk, J.:  
239 Coupled hydrogeophysical inversion of time-lapse surface GPR data to estimate hydraulic properties of a layered  
240 subsurface, *Water Resour. Res.*, 49(12), 8480–8494, doi:10.1002/2013WR013992, 2013.

241 Forte, E. and Pipan, M.: Review of multi-offset GPR applications: Data acquisition, processing and analysis, *Signal*  
242 *Processing*, 132, 1–11, doi:10.1016/j.sigpro.2016.04.011, 2017.

243 Gerhards, H., Wollschläger, U., Yu, Q., Schiwiek, P., Pan, X. and Roth, K.: Continuous and simultaneous  
244 measurement of reflector depth and average soil-water content with multichannel ground-penetrating radar,  
245 *Geophysics*, 73(4), 15–23, 2008.

246 Gloaguen, E., Chouteau, M., Marcotte, D. and Chapuis, R.: Estimation of hydraulic conductivity of an unconfined  
247 aquifer using cokriging of GPR and hydrostratigraphic data, *J. Appl. Geophys.*, 47(2), 135–152, doi:10.1016/S0926-  
248 9851(01)00057-X, 2001.

249 Guo, L., Chen, J. and Lin, H.: Subsurface lateral preferential flow network revealed by time-lapse ground-penetrating  
250 radar in a hillslope, *Water Resour. Res.*, 50, 9127–9147, doi:10.1002/2013WR014603, 2014.

251 Haarder, E. B., Looms, M. C., Jensen, K. H. and Nielsen, L.: Visualizing Unsaturated Flow Phenomena Using High-  
252 Resolution Reflection Ground Penetrating Radar, *Vadose Zo. J.*, 10(1), 84, doi:10.2136/vzj2009.0188, 2011.

253 Hendrickx, J. M. H. and Flury, M.: Uniform and Preferential Flow Mechanisms in the Vadose Zone, in *Conceptual*  
254 *Models of Flow and Transport in the Fractured Vadose Zone*, pp. 149–187, National Academy Press, Washington,  
255 D.C., 2001.

256 Irving, J. and Knight, R.: Numerical modeling of ground-penetrating radar in 2-D using MATLAB, *Comput. Geosci.*,  
257 32(9), 1247–1258, doi:10.1016/j.cageo.2005.11.006, 2006.

258 Jarvis, N., Koestel, J. and Larsbo, M.: Understanding Preferential Flow in the Vadose Zone: Recent Advances and  
259 Future Prospects, *Vadose Zo. J.*, 15(12), 0, doi:10.2136/vzj2016.09.0075, 2016.

260 Jarvis, N. J.: A review of non-equilibrium water flow and solute transport in soil macropores: Principles, controlling  
261 factors and consequences for water quality, *Eur. J. Soil Sci.*, 58(3), 523–546, doi:10.1111/j.1365-2389.2007.00915.x,  
262 2007.

263 Jaumann, S. and Roth, K.: Soil hydraulic material properties and subsurface architecture from time-lapse GPR,  
264 *Hydrol. Earth Syst. Sci. Discuss.*, (September), 1–34, doi:10.5194/hess-2017-538, 2017.

265 Klenk, P., Jaumann, S. and Roth, K.: Quantitative high-resolution observations of soil water dynamics in a complicated  
266 architecture using time-lapse ground-penetrating radar, *Hydrol. Earth Syst. Sci.*, 19(3), 1125–1139, doi:10.5194/hess-  
267 19-1125-2015, 2015.

268 Lafond, C. F. and Levander, A. R.: Migration moveout analysis and depth focusing, *Geophysics*, 58(1), 91–100,  
269 doi:10.1190/1.1443354, 1993.

270 Lambot, S., Antoine, M., van den Bosch, I., Slob, E. C. and Vanclooster, M.: Electromagnetic Inversion of GPR  
271 Signals and Subsequent Hydrodynamic Inversion to Estimate Effective Vadose Zone Hydraulic Properties, *Vadose*  
272 *Zo. J.*, 3(4), 1072, doi:10.2136/vzj2004.1072, 2004.

273 Lambot, S., Slob, E., Rhebergen, J., Lopera, O., Jadoon, K. Z. and Vereecken, H.: Remote Estimation of the Hydraulic  
274 Properties of a Sand Using Full-Waveform Integrated Hydrogeophysical Inversion of Time-Lapse, Off-Ground GPR  
275 Data, *Vadose Zo. J.*, 8(3), 743, doi:10.2136/vzj2008.0058, 2009.

276 Leparoux, D., Gibert, D. and Cote, P.: Adaptation of prestack migration to multi-offset ground-penetrating radar  
277 (GPR) data, *Geophys. Prospect.*, 49(3), 374–386, doi:10.1046/j.1365-2478.2001.00258.x, 2001.

278 Lunt, I. A., Hubbard, S. S. and Rubin, Y.: Soil moisture content estimation using ground-penetrating radar reflection  
279 data, *J. Hydrol.*, 307(1–4), 254–269, doi:10.1016/j.jhydrol.2004.10.014, 2005.

280 Mangel, A. R., Moysey, S. M. J., Ryan, J. C. and Tarbutton, J. A.: Multi-offset ground-penetrating radar imaging of  
281 a lab-scale infiltration test, *Hydrol. Earth Syst. Sci.*, 16(11), doi:10.5194/hess-16-4009-2012, 2012.

282 Mangel, A. R., Lytle, B. A. and Moysey, S. M. J.: Automated high-resolution GPR data collection for monitoring  
283 dynamic hydrologic processes in two and three dimensions, *Lead. Edge*, 34(2), doi:10.1190/tle34020190.1, 2015a.

284 Mangel, A. R., Moysey, S. M. J. and van der Kruk, J.: Resolving precipitation induced water content profiles by  
285 inversion of dispersive GPR data: A numerical study, *J. Hydrol.*, 525, 496–505, doi:10.1016/j.jhydrol.2015.04.011,  
286 2015b.

287 Mangel, A. R., Moysey, S. M. J. and van der Kruk, J.: Resolving infiltration-induced water content profiles by  
288 inversion of dispersive ground-penetrating radar data, *Vadose Zo. J.*, 16, doi:10.2136/vzj2017.02.0037, 2017.

289 Moysey, S. M.: Hydrologic trajectories in transient ground-penetrating-radar reflection data, *Geophysics*, 75(4),  
290 WA211-WA219, doi:10.1190/1.3463416, 2010.

291 Mualem, Y.: A new model for predicting the hydraulic conductivity of unsaturated porous media, *Water Resour. Res.*,  
292 12(3), 1976.

293 Neidell, N. S. and Taner, M. T.: Semblance and other coherency measures for multichannel data, *Geophysics*, 36(3),  
294 482–497, 1971.



295 Nimmo, J. R.: Preferential flow occurs in unsaturated conditions, *Hydrol. Process.*, 26(5), 786–789,  
296 doi:10.1002/hyp.8380, 2012.

297 Saintenoy, A., Schneider, S. and Tcholka, P.: Evaluating GroundPenetrating Radar use for water infiltration  
298 monitoring, 2007 4th Int. Work. on, *Adv. Gr. Penetrating Radar*, 91–95, doi:10.1109/AGPR.2007.386531, 2007.

299 Sava, P. and Biondi, B.: Wave-equation migration velocity analysis. I. Theory, *Geophys. Prospect.*, 52(6), 593–606,  
300 doi:10.1111/j.1365-2478.2004.00447.x, 2004a.

301 Sava, P. and Biondi, B.: Wave-equation migration velocity analysis — II : Subsalt imaging examples Geophysical  
302 Prospecting , accepted for publication, , 1–36, 2004b.

303 Simunek, J. and van Genuchten, M. T.: HYDRUS code for simulating the movement of water, heat, and multiple  
304 solutes in variably saturated porous media, 2005.

305 Steelman, C. M. and Endres, A. L.: An examination of direct ground wave soil moisture monitoring over an annual  
306 cycle of soil conditions, *Water Resour. Res.*, 46(11), n/a-n/a, doi:10.1029/2009WR008815, 2010.

307 Stork, C.: Reflection tomography in the postmigrated domain, *Geophysics*, 57(5), 680–692, doi:10.1190/1.1443282,  
308 1992.

309 Topp, G. C., Davis, J. L. and Annan, A. P.: Electromagnetic Determination of Soil Water Content:, *Water Resour.*  
310 *Res.*, 16(3), 574–582, 1980.

311 Vellidis, G., Smith, M. C., Thomas, D. L. and Asmussen, L. E.: Detecting wetting front movement in a sandy soil  
312 with ground-penetrating radar, *Am. Soc. Agric. Eng.*, 33(6), 1867–1874, 1990.

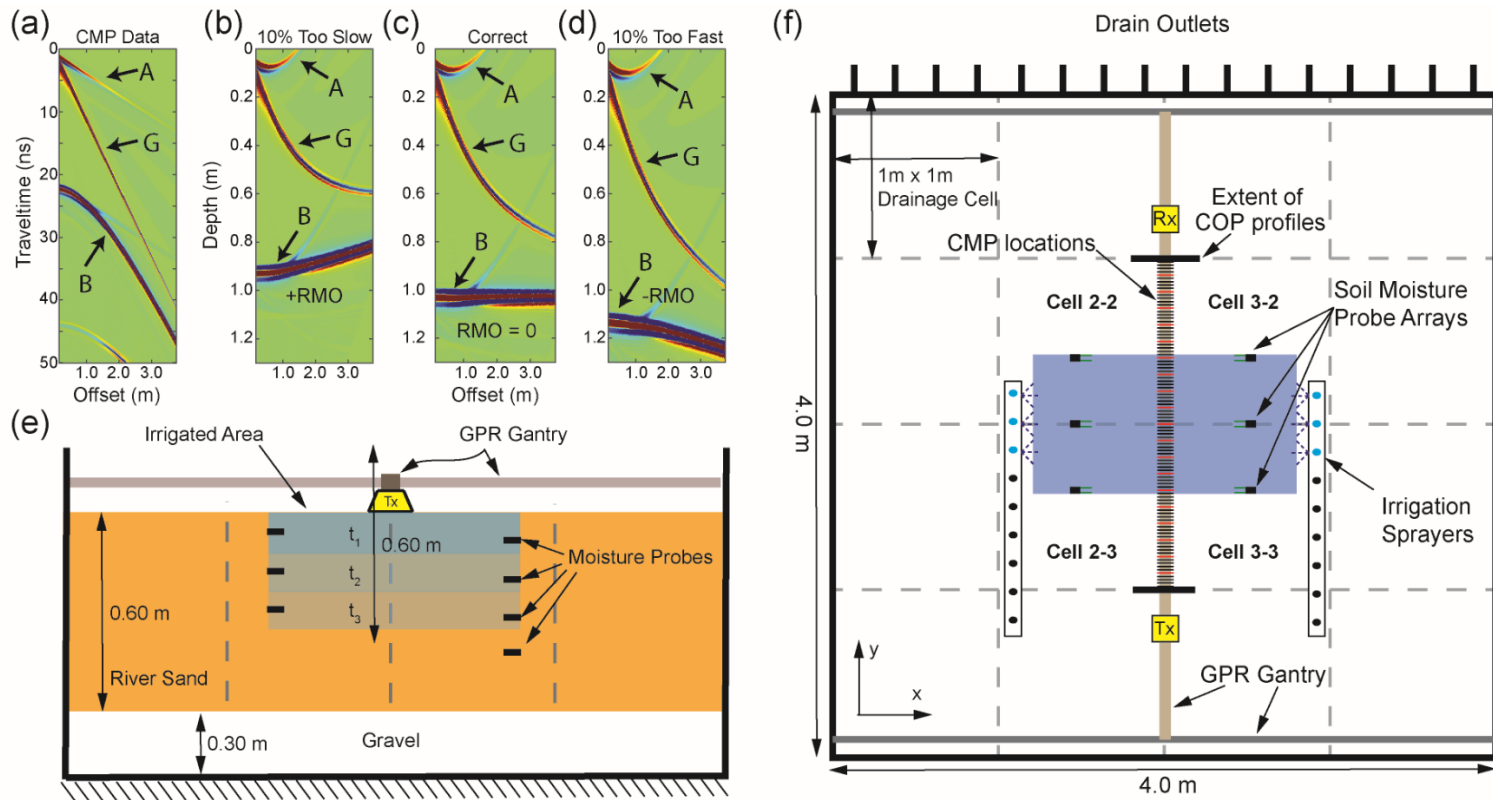
313 Yilmaz, O. and Chambers, R.: Migration velocity analysis by wave-field extrapolation, *Geophysics*, 49(10), 1664–  
314 1674, 1984.

315 Yilmaz, O. and Doherty, S.: *Seismic Data Analysis: Processing, Inversion, and Interpretation of Seismic Data*, 2nd  
316 ed., Society of Exploration Geophysicists, Tulsa, OK., 2001.

317

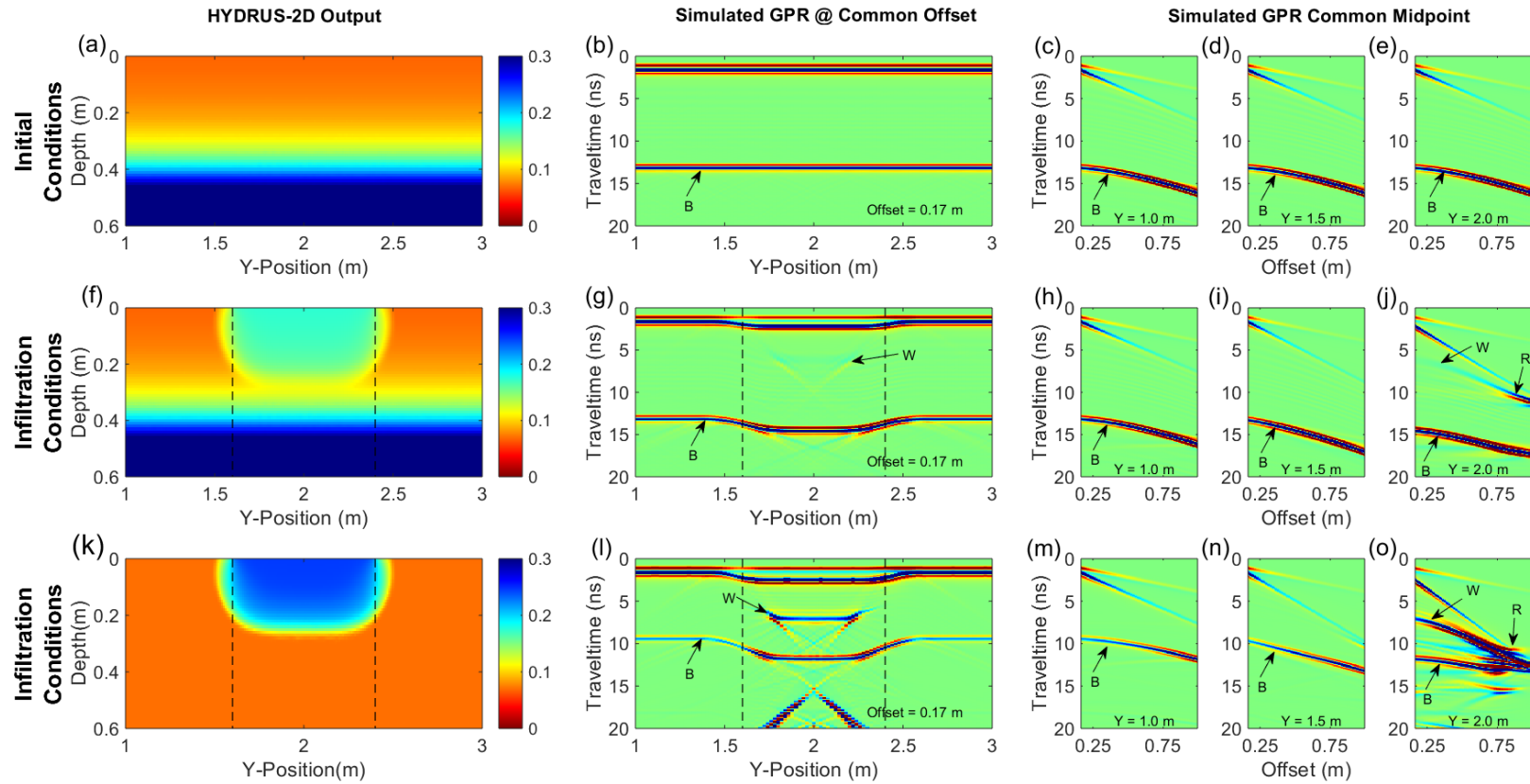
318 **8. Figures**

319 **Figure 1**

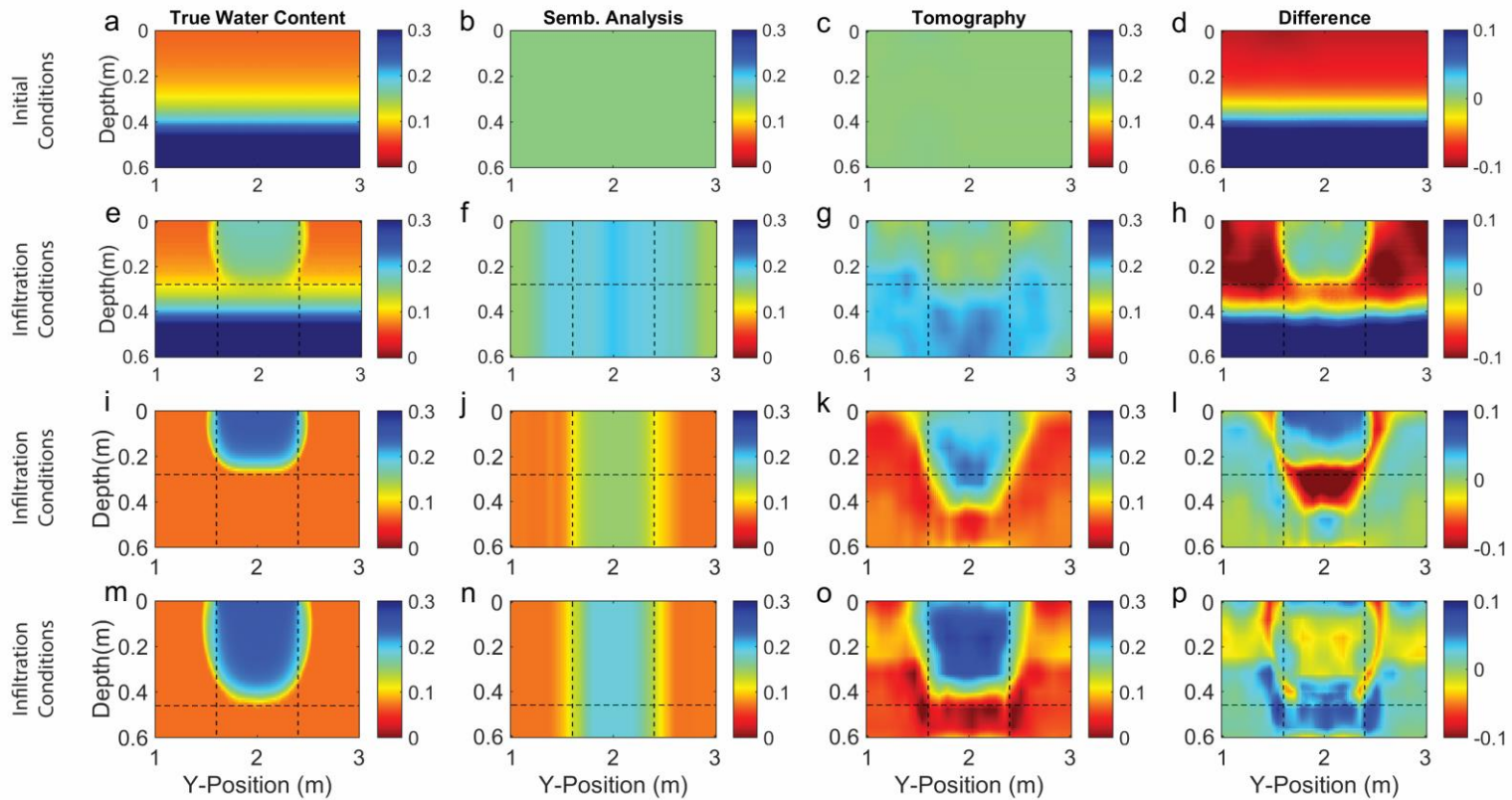


320

321 Figure 1: a) Example CMP data showing the airwave (A), groundwave (G) and reflection from a layer (B). Data in (a) is migrated to form (b) a migrated gather  
 322 with velocity 10% slow; c) a migrated gather with correct velocity; and d) a migrated gather with velocity 10% fast. Panel (e) shows a cross-section of the experiment  
 323 at  $y = 2.0$  where  $t_1$ ,  $t_2$ , and  $t_3$  are arbitrary times during the infiltration. Panel (f) shows the plan-view of the experiment. Note that the bottom of the sand layer is  
 324 flat where GPR data collection occurs, i.e. on a boundary between drain cells, and pitched elsewhere toward cell drains.



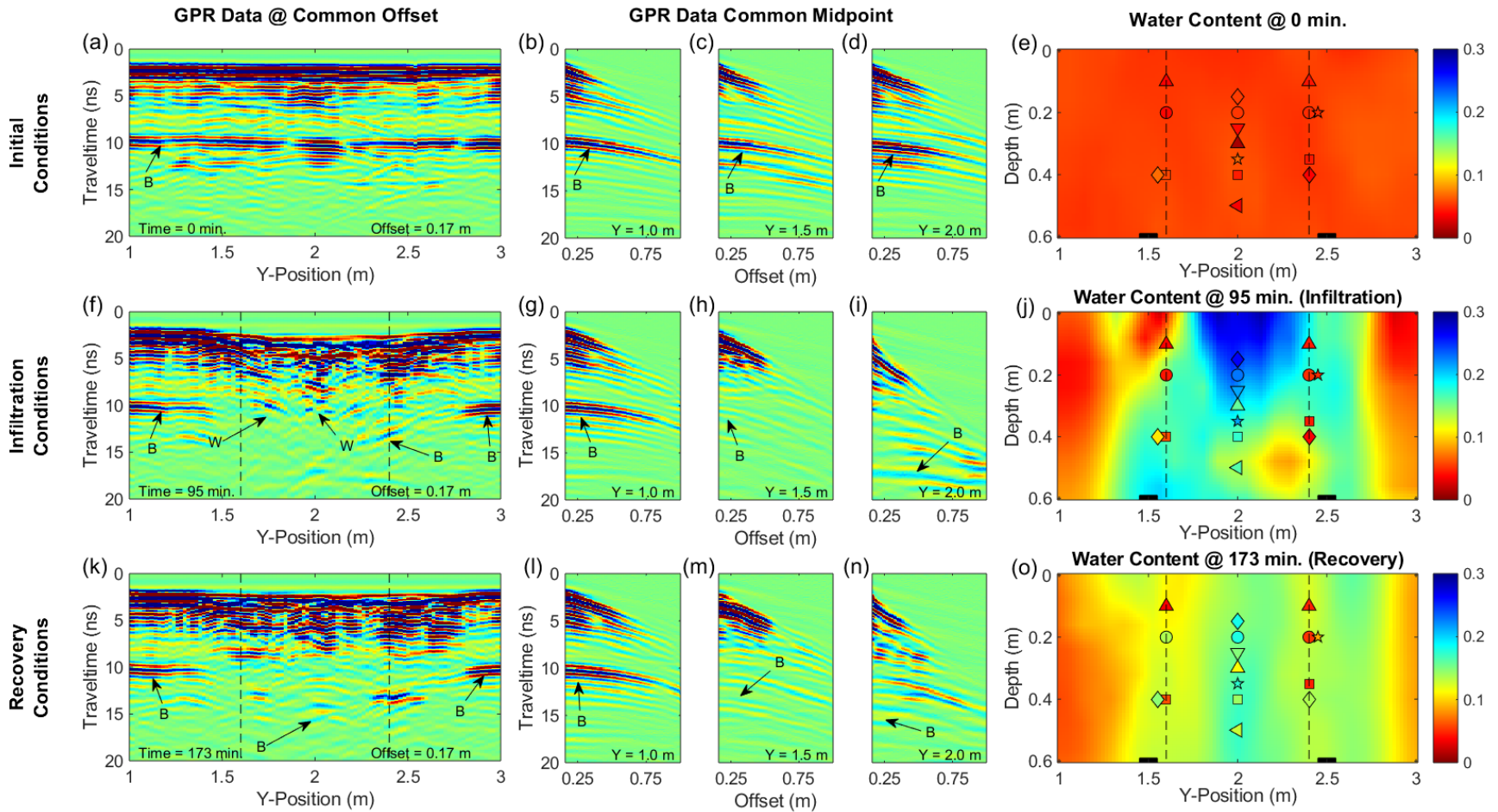
327 Figure 2: Panels (a), (f), and (k) show volumetric moisture distribution from HYDRUS-2D simulations used to generate simulated common-offset GPR data (b, g,  
 328 l) and multi-offset GPR data (c-e, h-j, and m-o). Vertical dashed lines indicate the extent of the wetted surface. Annotated arrivals are the bottom of sand layer  
 329 reflection (B), wetting front reflection (W), and refraction (R). Note that the base of sand reflection (B) is caused by the boundary at 0.60 m depth between the sand  
 330 and gravel, not the capillary rise shown in panels (a) and (f).



332

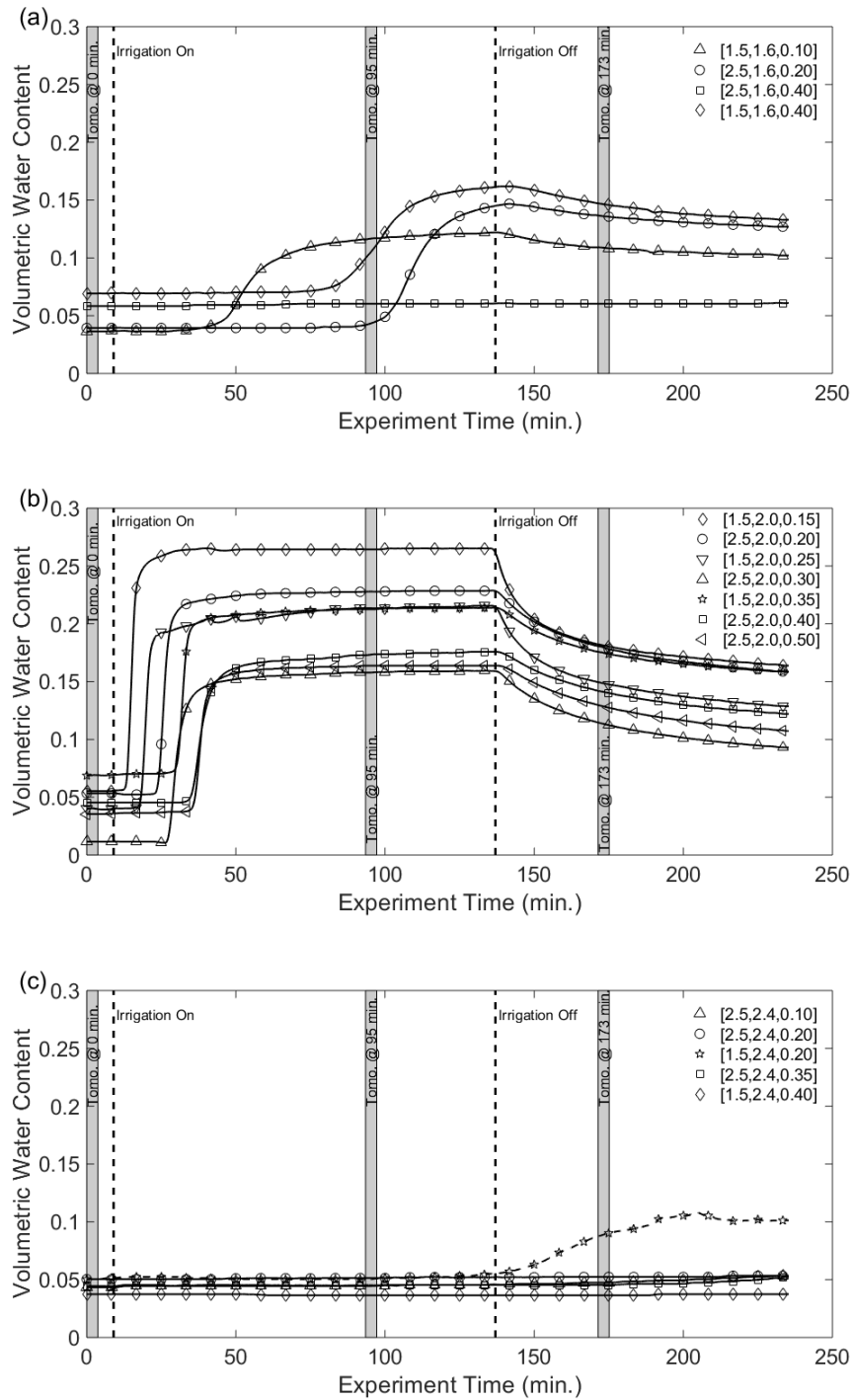
333 Figure 3: Panels (a), (e), (i), and (m) show true volumetric water content distributions from HYDRUS-2D. Panels (b), (f), (j), and (n) show starting models for the  
 334 tomography derived from semblance analysis. Panels (c), (g), (k), and (o) show results of tomography of the simulated GPR data as volumetric water content.  
 335 Difference plots (d), (h), (l), and (p) were calculated by subtracting the tomography results from the true water content distributions; red areas indicate volumetric  
 336 moisture overestimation while blue areas indicate volumetric moisture underestimation.

337



339

340 Figure 4: Panels (a, f, and k) are common-offset GPR data collected during the experiment. Panels (b-d, g-i, and l-n) are CMP data collected during the experiment.  
 341 Arrivals annotated are the sand layer reflection (B) and wetting front reflection (W). Panels (e, j, and o) show tomography results for the corresponding GPR data.  
 342 Vertical lines indicate the lateral extent of the wetted surface. Shapes correspond to the soil moisture data for the given y-location in Figure 5, colors correspond to  
 343 the measured soil moisture. Adjacent symbols are from probes that are located at different x-locations, but identical depths.



345  
 346 Figure 5: Soil moisture probe data from the in-situ moisture probes along the GPR line at a)  $y = 1.6$  m; b)  $y = 2.0$  m;  
 347 and c)  $y = 2.4$  m. Vertical dashed lines indicate the start and stop of irrigation. Gray bars indicate the times when data  
 348 in Figure 4 were collected. Symbols for a given data set match those on Figures 4e, j, and o. Soil moisture data were  
 349 collected 60 minutes beyond the end of GPR data collection.